ACS ES&T Engineering

pubs.acs.org/estengg

Article

Optimizing a Cogeneration sCO_2 CSP−MED Plant Using Neural Networks

Rodrigo A. Caceres Gonzalez, Yanjie Zheng, Kelsey B. Hatzell, and Marta C. Hatzell*

Cite This: *ACS EST Engg.* 2021, 1, 393−403

Read Online

ACCESS | Metrics & More | Article Recommendations | Supporting Information

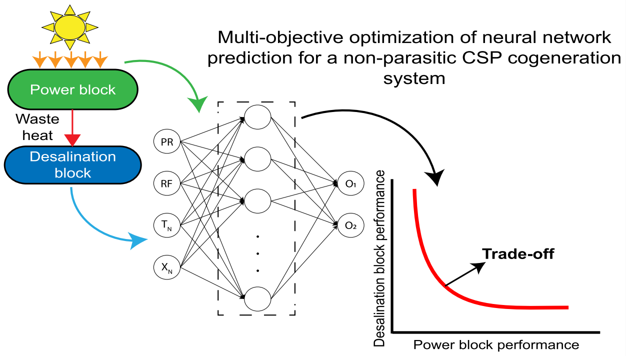

ABSTRACT: Defining optimal cogeneration system design requires the use of complex analyses capable of capturing dynamic processes within multiple subsystems and individual devices in parallel. This is due to the well-known fact that optimal cogeneration system performance does not always correlate with the optimal performance of a single subsystem. Furthermore, subsystems and single devices often present inherent design trade-offs which are not easily captured in subsystem level models. Here, we perform a steady state thermodynamic and economic analysis for a concentrated solar power (CSP) cogeneration system producing power through a supercritical carbon dioxide (sCO_2) Brayton cycle and water through a multieffect distillation (MED) plant. The use of three artificial neural networks allows for the prediction of economic performance (levelized cost of water and electricity) and system performance (thermal efficiency, second law efficiency, performance ratio, and solar performance ratio). The cogeneration system results in a higher levelized cost of electricity (LCOE) than state-of-the-art CSP sCO_2 plants. However, this reduction in power performance allows for a levelized cost of water of 1.1 $\$/m^3$, which is comparable to conventional membrane-based processes (1.25 $\$/m^3$) and significantly less than other solar thermal (1.8 $\$/m^3$) desalination systems. The nonparasitic integration between the sCO_2 Brayton cycle and MED plant also allows for maximization of water production without altering the second law efficiency of the cogeneration system, which remains at 11% during the analysis.

KEYWORDS: *cogeneration systems, sCO_2 power cycles, thermal desalination, multiobjective optimization, neural networks*

■ INTRODUCTION

Water scarcity and stress projections indicate that there is an increasing demand for freshwater.[1] Seawater desalination can minimize this challenge, as 97% of the total water availability resides in oceans. Today, most seawater desalination occurs through membrane (reverse osmosis) or through thermal separation (evaporation).[2] Both approaches are equally effective for desalinating seawater; however, seawater reverse osmosis (SWRO) has a specific equivalent energy consumption (SEC_{equiv}) (estimation of SEC_{equiv} explained in the Supporting Information) of 1.58−7.5 kW h/m^3, while thermal desalination systems report SEC_{equiv} which range from 10 to 35 kW h/m^3.[3] The high SEC_{equiv} is limited by the unique thermodynamic properties of water (high heat capacity), resulting in a large energy demand for phase change. For this reason, RO accounts for 65% of the desalination market while thermal processes (multistage flash and multieffect distillation) only account for 28%.[4,5]

Fossil fuel energy sources supply nearly all (99%) the energy for desalination processes mainly due the higher costs associated with fully integrated renewable desalination systems.[6] This trend however cannot continue, as it is projected that globally installed desalination plants will produce 218 million tons of CO_2 by 2040 if the business-as-usual scenario remains.[6] Thus, integrating renewables such as solar with desalination plants is of particular interest to mitigate carbon emissions.[7,8]

There are two main solar energy integration strategies for desalination: direct and indirect systems. Direct solar desalination refers to any thermal process where solar capture and desalination occur within the same system. Examples include solar-driven water vaporization systems (solar stills and other photothermal materials). While direct integration creates intensified processes, ultimately they suffer from low rate of production (≤ 100 m^3/day), low performance (gain output ratio, GOR < 1), and high cost (levelized cost of water, LCOW up to 6.5 $\$/m^3$).[4,9] Indirect solar desalination refers to any system where the subsystems (solar capture and desalination) operate independently and are connected through an

Received: September 7, 2020
Revised: November 3, 2020
Accepted: November 9, 2020
Published: November 20, 2020

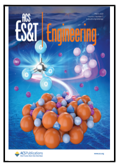

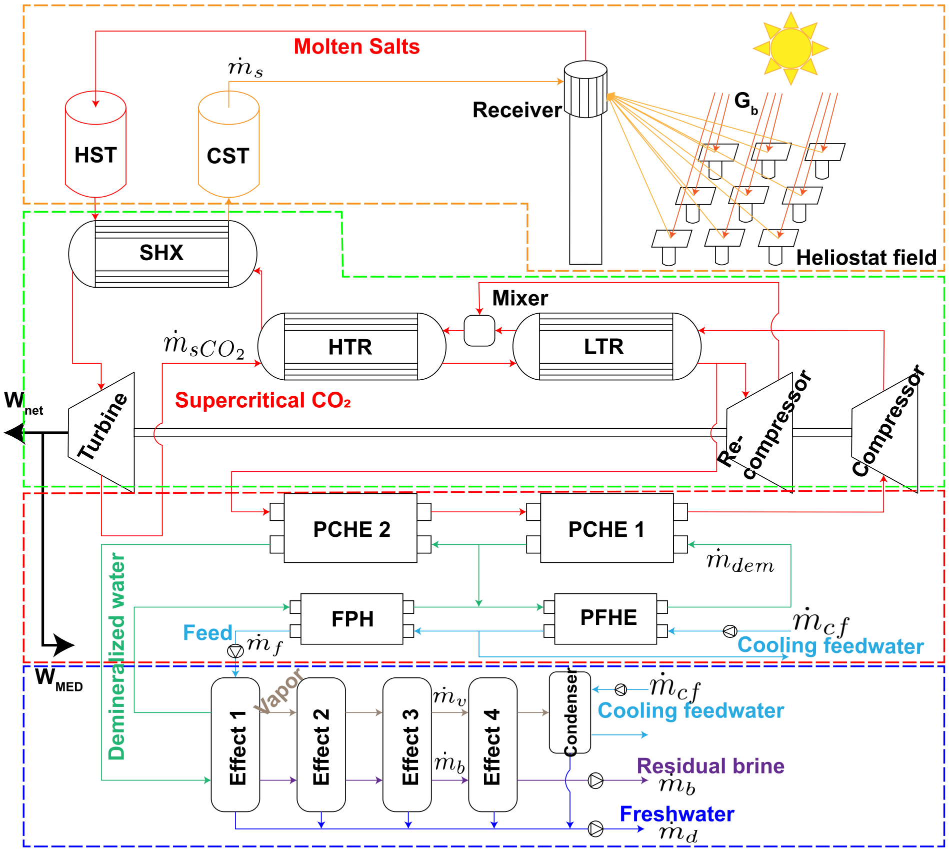

Figure 1. Diagram for the integrated cogeneration system divided in four principal blocks based on the literature work.[21] The region highlighted by the orange dotted box is the solar block using molten salts ($\dot{m}_s$) as the heat transfer fluid, and the region highlighted by the green dotted box is the power block using supercritical carbon dioxide ($\dot{m}_{sCO_2}$) as the working fluid; the region highlighted by the red dotted box is the integration block using demineralized water ($\dot{m}_{dem}$) as the heat transfer fluid, and the region highlighted in the blue dotted box is the desalination block using seawater ($\dot{m}_{sea}$) as the working fluid which is divided into feed, brine, vapor, and distilled ($\dot{m}_f$, $\dot{m}_b$, $\dot{m}_v$, and $\dot{m}_d$).

integration subsystem. One promising indirect route heavily investigated is photovoltaics (PV) with RO (PV-RO). This is promising as the cost of PV has significantly dropped over the past few decades, and the temperature match between systems (near ambient) allows for ease of integration.[10] However, despite the promise, PV-RO systems still suffer from higher cost (11.7−15.6 \$/m^3).[4] While some of this high cost can be mitigated through increasing the production volumes, this current price is not competitive when compared to fossil driven desalination-based systems.[4] Furthermore, the current cost for PV-RO is also more expensive than solar−thermal integration (concentrated solar power−multieffect distillation, CSP−MED) strategies which have been shown to attain prices which approach 2.4−2.8 \$/m^3 while producing more than 5000 m^3 of water per day.[4]

Thus, in an effort to meet both production and cost demands, solar−thermal indirect cogeneration (power and water) systems are gaining interest. Colocating power and water is potentially also ideal as power systems heavily rely on water for cooling, and thus, access to water would no longer limit power plant location or operation time. Cogeneration power and water systems are also advantageous as it would allow a desalination plant to operate independent of the electricity grid. With rising concerns with outdated electrical grid-based infrastructure, reducing rather than adding loads is advantageous.[6,11] Realization of solar power and water could ultimately mitigate many issues at the center of the water-energy nexus.

The most likely approach to achieve solar−thermal indirect cogeneration of solar and water requires the use of CSP with thermal desalination (MED). While CSP systems still operate at temperatures well beyond that of thermal desalination systems, this approach can help in decreasing the temperature mismatch between the power and desalination system through the use of waste heat. Temperature match between subsystems allows for less heat exchange loss. CSP−MED driven by a supercritical CO_2 (sCO_2) Brayton cycle has been investigated and shown to decrease the cost of energy (LCOE) by 18%, when compared to a steam-driven Rankine cycle (LCOW remained fixed).[12] This improvement in performance is due to the unique recompression Brayton cycle which can operate with higher efficiencies due the higher temperature (> 600 °C) when compared with traditional steam cycles (≈550 °C).[13−16] A secondary benefit is that the integration is nonparasitic (i.e., power cycle efficiency is not influenced by the desalination system). Others have investigated sCO_2 CSP−MED systems to meet municipal scale demands.[17,18]

Despite the current work in the field, there is a further need to expand these analyses to identify the operational trade-offs which exist between the power and desalination subsystems, in order to maximize system performance under a range of conditions relevant for operation for direct seawater desalination or inland applications. The complexity of a cogeneration system modeling and optimization represents a major issue for computational resources consumption. Artificial neural networks (ANNs) allow for a reduction in simulation time through the use of a simplified estimation of solutions to highly complex nonlinear thermodynamic and economic functions which typically require iterative solvers.[19,20] The advantage of ANN approaches for optimization is that the predictions are based on input data and not mathematically constrained. Each ANN can be represented as a polynomial function based on input parameters which is easier to optimize.

Through identifying and predicting the most influential system parameters, we aim to determine which systems metrics are most suitable for evaluating the performance of a solar cogeneration system using machine learning as a tool for reduced computational time consumption. We aim to examine the sensitivity that levelized cost (electricity and water) and production (energy and water) have on system performance (recovery ratio, thermal efficiency, gain output ratio (GOR)) considering the operation of the cogeneration system.

SYSTEM DESCRIPTION

The cogeneration system is composed of four blocks: solar tower block, power block, integration block, and desalination block. The desalination block uses waste heat from the power block as the primary energy source, without influencing the power block efficiency (Figure 1).[21] For the solar tower block (components enclosed in orange dotted square in Figure 1), the heliostat field captures the incident irradiance (G_b) concentrating sunlight into a central receiver tower. The receiver heats a molten salt stream ($\dot{m}_s$) which then is stored within a hot storage tank (HST). Heated molten salts then exchange heat with a supercritical carbon dioxide ($\dot{m}_{sCO_2}$) stream through the salt heat exchanger (SHX). A cold storage tank (CST) stores the exhaust molten salts from the SHX before circulating back to the receiver.

In the power block (components enclosed in the green dotted square in Figure 1), the heated sCO_2 expands in the turbine producing the power ($\dot{W}_t$) which drives the compression devices in the power, integration, and the desalination blocks ($\dot{W}_C$, $\dot{W}_{RC}$, and $\dot{W}_{MED}$). The remaining power ($\dot{W}_{net}$) is available for delivering on the electrical grid. The low-pressure exit sCO_2 from the turbine preheats the high-pressure sCO_2, before entering the SHX, through a high- and a low-temperature recuperator (HTR and LTR). The exhaust low-pressure flow leaving the LTR divides into two streams as a function of the recompression factor (RF) of the Brayton cycle. A fraction (RF) of the sCO_2 flows to the recompressor, and the remaining (1 − RF) flows to the integration block for cooling.

The integration block (components enclosed in the red dotted square in Figure 1) cools the exhaust sCO_2 from the LTR to the compressor inlet temperature and simultaneously provides heat to the desalination block through two printed-circuit heat-exchanger devices ($PCHE_1$ and $PCHE_2$) using a demineralized water stream ($\dot{m}_{dem}$).[17] The cooling process aims at maximizing the temperature of the demineralized water stream, which is used to supply the required thermal energy to perform desalination ($\dot{Q}_{MED}$). After transferring heat to the desalination block, the demineralized water stream enters the feed preheater (FPH) and then mixes with the demineralized flow that does not enter the $PCHE_2$. To reach the temperature required to cool the sCO_2 stream in the $PCHE_1$, demineralized water rejects heat to feedwater in a plate and frame heat exchanger (PFHE). A fraction of the feedwater stream, used for cooling the demineralized water, flows to the FPH as feed.

The desalination block (components enclosed in the blue dotted square in Figure 1) has a forward feed flow configuration, which for sensible heat sources reaches higher productivity compared with parallel flow schemes.[18] The first effect uses the demineralized water heated in the $PCHE_2$ as heat source to evaporate part of the feed ($\dot{m}_f$) supplied from the FPH. This process produces two outcomes, vapor ($\dot{m}_v$) and brine ($\dot{m}_b$). Both streams are inputs of the subsequent MED effects. Freshwater production occurs from the condensation of the vapor flowing from one effect to another. Heat is transferred to the brine, and the vapor is transferred to the next effect, as an energy driver for the next effects. In the condenser, vapor produced in the last effect condenses rejecting heat ($\dot{Q}_{cond}$) to a feedwater stream and then mixes with the freshwater stream ($\dot{m}_d$) produced in previous stages. The desalination block requires electricity for running the pumps used for ensuring the flow of feedwater, brine, and freshwater along the desalination block ($\dot{W}_{MED}$).

METHODOLOGY

A thermodynamic model was built to identify energy flows within each subsystem and device. The model allows for analyses to be performed on single subsystems or the complete cogeneration system. This enables the identification of relevant subsystem operating conditions and fluid properties, which influence cogeneration system performance metrics. The primary model inputs for the power block subsystem are pressure ratio (PR) and recompression factor (RF). The turbomachinery inlet temperature (TIT, CIT, and RCIT for turbine, compressor, and recompressor), isentropic efficiency (η_t, η_c, and η_{rc}), and recuperator effectiveness (ε) are constants throughout the analyses. Different than TIT, PR and RF have a direct influence in the power block efficiency being inversely related and also affecting the heat rejection section and sCO_2 flow in the system, which is variable due the TIT constant value assumption (Figures S1−S3). Lower pressure and compressor inlet temperature remains constant to ensure CO_2 in the supercritical state flowing in the system during all the analyses (Table S3). For the desalination block subsystem, the number of effects (N), last effect temperature (T_N), feed and brine salinity (X_f and X_N), temperature difference between effects ($\Delta T_{effects}$), and cooling feedwater in the condenser (ΔT_{cond}) are the input parameters (Table S4) with the last effect temperature and residual brine salinity as main variables since they can influence more in the standalone desalination block performance and recovery ratio compared with number of effects (Figures S4 and S5). The feed salinity is defined as 33.5 g/kg. The model outputs are the power block thermal efficiency (η_{PB}), the desalination block performance ratio (PeR), the cogeneration system second law efficiency ($\eta_{II,system}$), and solar performance ratio (SolarPerR). These performance metrics allow for the determination of the capital and operation costs for each component, subsystem, and the entire cogeneration plant, allowing for the determination of the levelized cost of water and electricity (LCOW and LCOE).

The solar field was simulated through System Advisor Model (SAM).[22] SAM optimizes the solar field for a desired power cycle, given irradiance, location, and objective thermal efficiency for a CSP system. SAM simulation outputs include heliostat field area, solar field efficiency, molten salt tank temperature, and solar field costs. For the annual irradiance profile and environmental conditions, SAM uses the data available for Dagget, CA, with 10 h of thermal storage and 850 W/m^2 of irradiation for base conditions (same as San Diego, CA, close to the sea location, Table S2). Evaluating a yearly operation, SAM provides the capacity factor (CF) of the cogeneration system, which is equal to the capacity factor of the solar block. Engineering Equation Solver (EES) provides fluid properties and solves the energy and mass balance through each device contained in the power block subsystem, integration block subsystem, and desalination block subsystem. EES relies on an external library in order to calculate saline feedwater thermophysical properties including boiling point elevation (BPE), enthalpy, entropy, and Gibbs free energy as a function of pressure, temperature, and concentration.[23−25]

For an optimal operation in the heat rejection from the power block, the use of two PCHE devices is necessary, where the higher amount of heat must be dissipated in the devices that supply cool sCO_2 to the compressor.[17] Here, for optimal operation based on the validation point system,[21] 1/3 of exhaust heat is rejected by the sCO_2 stream in the $PCHE_2$ ($(1 - RF) \times \dot{m}_{sCO_2}$), heating the demineralized water flowing to the desalination block ($\dot{m}_{dem,in,MED}$), while the remaining heat is dissipated in the $PCHE_1$ so the sCO_2 stream reaches the compressor inlet temperature.[17] The heat exchange process between sCO_2 and the demineralized water stream in both PCHE devices is isobaric and nonisothermal. While the specific heat of demineralized water is assumed constant (4.18 kJ/(kg K)), specific heat of CO_2 is nonlinear with changes in temperature and pressure when operating near the critical point.[26] To evaluate the energy balance inside each PCHE device considering the change of CO_2 specific heat with variation in temperature, the heat transfer process between these two fluids inside the $PCHE_1$ and $PCHE_2$ is parametrized in 10 and 5 points considering a pinch point temperature of 3 °C inside each one (Figure S6). The parametrization maximizes the temperature of the demineralized flow in the integration block flowing into the desalination block. The demineralized water achieves the closest temperature to sCO_2 even with a fixed heat rejection fraction (Figure S7). The volume of feed saline water stream entering the desalination block depends on the heat transferred from the power block and the water recovery ratio (Equation S16). Here, the water recovery varied, in order to maximize heat rejection from the power block and subsequently the temperature of the demineralized water stream entering the desalination block. Each effect has a fixed operational temperature difference of 3 °C for ensuring driving forces and is also considered a 1 °C additional for thermodynamic losses and nonequilibrium allowance (NEA).[21,27] The cooling feedwater stream in the condenser has a fixed temperature difference of 5 °C. The cogeneration system validation compares with results available in the literature of the power and water production when the power block operates at maximum thermal efficiency producing 113.5 MW of power and 30.8 kg/s of water (Table S5).[21] The power block was validated standalone compared with results reported in the literature (Figure S11).[13]

Performance Metrics. The most critical economic metrics used to evaluate performance are the levelized costs of electricity and water (LCOE and LCOW). These are a function of total annual production (power and water) and annualized capital, operation, and maintenance cost:

$$\mathrm{LCOE} = \frac{\mathrm{CRF} \times \mathrm{CC} + \mathrm{O\&M}_{\mathrm{annual}}}{\dot{W}_{\mathrm{annual}} \times \mathrm{CF}} \left[\frac{\$}{\mathrm{kW\,h}}\right] \tag{1}$$

$$\mathrm{LCOW} = \frac{\mathrm{CRF} \times \mathrm{CC} + \mathrm{ChC}_{\mathrm{annual}} + \mathrm{LaC}_{\mathrm{annual}} + \mathrm{O\&M}_{\mathrm{annual}}}{\mathrm{Water}_{\mathrm{annual}} \times \mathrm{CF}} \left[\frac{\$}{\mathrm{m}^3}\right] \tag{2}$$

$$\mathrm{CRF} = \frac{k_d \cdot (1 + k_d)^{yrs}}{(1 + k_d)^{yrs} - 1} \tag{3}$$

where $\mathrm{ChC}_{\mathrm{annual}}$ is the annualized chemical costs, $\mathrm{LaC}_{\mathrm{annual}}$ the annualized labor annualized costs, CF the capacity factor, a function of solar plant availability and estimated by SAM (48.9% in this work), and CRF the capital recovery factor applied for annualizing the total capital costs expenditures (CC) of the system, where the discount rate (k_d) and the lifetime of the system (years) are 8% and 25 years.[21]

Capital cost correlations for turbomachinery are highly dependent on the pressure ratio and the mass flow through the device (Equations S18−S20) while the heat exchangers' capital cost depends mainly on the overall heat transfer coefficient (U) and area (A) (Equations S25−S27). Operation and maintenance costs ($\mathrm{O\&M}_{\mathrm{annual}}$) for the solar and power block are a fixed percentage of capital expenditures (15%).[28,29] For LCOE, the capital expenditure includes costs of the solar field (Table S2) and both PCHE devices, while the costs of the remaining heat exchanger devices in the integration block are allocated in the LCOW calculation. Desalination block annualized cost calculations include annualized costs for chemicals and labor (0.025 and 0.1 $\$/m^3$) along with operation and maintenance costs fixed as 2% of the capital expenditure costs.[30]

For individual block metrics, the performance of a power cycle is evaluated by the thermal efficiency. For the standalone power block thermal efficiency (eq 4), the net power ($\dot{W}_{\mathrm{net,PB}}$) considers the turbine driving only power block compression devices. The heat supplied is the heat transferred in the salt heat exchanger ($\dot{Q}_{\mathrm{SHX}}$).

$$\eta_{\mathrm{PB}} = \frac{\dot{W}_{\mathrm{net,PB}}}{\dot{Q}_{\mathrm{SHX}}} [-] \tag{4}$$

In evaluating the standalone performance of the desalination block, gain output ratio (GOR) or conventional performance ratio is not suitable, since the optimal value for these metrics is not congruent with maximum water production.[31] The corrected or waste heat performance ratio (called PerR for simplicity) considered in this work is defined as the total produced freshwater water evaporation energy over the maximum available energy from the heat source.[31,32]

$$\mathrm{PerR} = \frac{\dot{D} \times h_{\mathrm{ref}}}{\dot{m}_{\mathrm{dem,in,MED}} \times \mathrm{cp}_{dem}(T_{\mathrm{in,MED}} - T_0)} [-] \tag{5}$$

where h_{ref} is the distillate specific reference enthalpy (2336 kJ/kg). The maximum available energy depends on the flow rate of demineralized water, the temperature of the stream leaving the $PCHE_2$, and the seawater temperature (assumed to be T_0).

For system metrics, the second law efficiency of the cogeneration system considers that the power block drives the compression devices in the desalination block ($\dot{W}_{\mathrm{MED}}$). Power consumption is a function of the mass flow, efficiency, and head (Equation S17 and Table S1).[33] Power and exergy of the freshwater stream are the products of the system, while exergy of the brine and cooling seawater streams is lost exergy.

$$\eta_{\text{II,system}} = \frac{\dot{W}_{\text{net,system}} + \dot{D}\cdot\psi_{\text{dist}}}{\dot{\chi}_{\text{sun}}}\ [-] \tag{6}$$

where $\dot{\chi}_{\text{sun}}$ is the total solar exergy provided by the solar block estimated using a very common correlation available in the literature.[34]

$$\dot{\chi}_{\text{sun}} = G_{\text{b}} \times A_{\text{hel}} \times \left[1 - \left(\frac{4}{3}\right)\left(\frac{T_0}{T_{\text{sun}}}\right) + \left(\frac{1}{3}\right)\left(\frac{T_0}{T_{\text{sun}}}\right)^4\right] \tag{7}$$

where A_{hel} is the total area of the heliostat field reflecting irradiance G_{b}, and T_{sun} is the effective temperature of the sun equal to 5777 K.

Exergy of the freshwater stream only considers the thermomechanical portion while chemical exergy is neglected due to nonvariation in the chemical composition of freshwater.

$$\psi_{\text{dist}} = (h_{\text{dist}} - h_0) - T_0 \times (s_{\text{dist}} - s_0) \tag{8}$$

Here, h_0 and s_0 are the enthalpy and entropy of water at T_0 = 20 °C and P_0 = 100 kPa. A modified performance ratio, denominated solar performance ratio (SolarPerR), compares the energy used for evaporating freshwater against the total solar energy input to the system.

$$\text{SolarPerR} = \frac{\dot{D} \times h_{\text{ref}}}{G_{\text{b}} \times A_{\text{hel}}}\ [-] \tag{9}$$

Here, h_{ref} is the benchmark value used in performance ratio calculations (2336 kJ/kg). Solar performance ratio evaluates the potential of the cogeneration system as a whole for converting input energy (solar) into freshwater. Therefore, it is a global performance metric unlike performance ratio (PerR), which only evaluates the performance of the desalination block converting waste heat into freshwater. Thus, it is a system metric that is suitable for contrasting with second law efficiency in a multiobjective optimization.

■ MULTIOBJECTIVE OPTIMIZATION USING NEURAL NETWORKS

The proposed cogeneration system produces power and freshwater. The developed thermodynamic model indicates that varying PR and RF to maximize η_{PB} maximizes $\eta_{\text{II,system}}$. This is due to the fact that the exergy of produced freshwater in the desalination block is three orders of magnitude lower when compared with net power production, making the power block the main influential subsystem in the cogeneration system exergetic efficiency (122 444 kW and 135.4 of exergy for net power and freshwater produced at maximum second law efficiency of the cogeneration system). Analyzing efficiency equations for the power block and cogeneration system, the heat and exergy input does not vary with changes in PR or RF, but only power and distillate (eqs 4 and 6). For RF = 0.366, increasing PR from the optimal point (3.5) increases water production but decreases net power production showing a trade-off between products of the cogeneration system in second law efficiency (Figure 2).

Exploring this or other trade-offs, through a multiobjective optimization, aids in visualizing the influence that simultaneous system properties have on defining an optimal design based on desired output conditions. Due to limitations of EES in multiobjective optimization, the weighted method or direct optimization is used most frequently when analyzing power cycles, desalination plants, and cogeneration systems.[35−38] However, the computational resources and time consumption with high system complexity often prevent convergence. The use of an artificial neural network (ANN) can address this problem associated with processing complex models in order to predict system performance with high accuracy.[39]

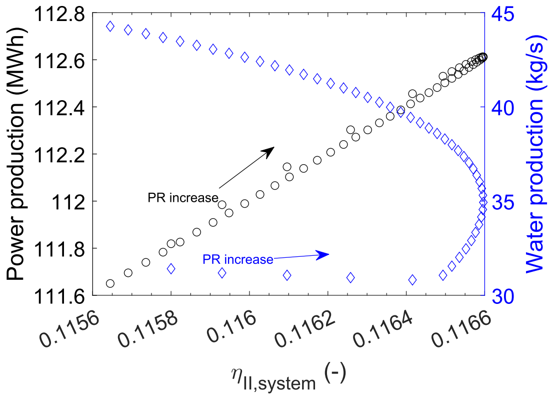

Figure 2. System second law efficiency and production levels for different PR with its optimal RF maximizing power block thermal efficiency.

Optimization Process. The complete optimizations require the integration and communication between EES and Matlab (Figure S8). The thermodynamic model created in EES provides input data through a parametric analysis varying four operational parameters that influence the performance of the power and desalination block (PR, RF, T_N, and X_N) and calculating the six metrics (LCOE, LCOW, η_{PB}, PerR, $\eta_{\text{II,system}}$, SolarPerR). Here, 160 000 data points are obtained varying PR from 3.1 to 5, RF from 0.25 to 0.44, T_N from 35 to 45 °C, and X_N from 57 to 95 g/kg. The Neural Network Toolbox available in Matlab creates and trains the neural network using this input data. Raw input data are normalized in the range [−1, 1] automatically and randomly divided for training (60%), validation (20%), and testing (20%). Each one of the three generated networks has one hidden layer (also called the Perceptron) with 4, 65, and 2 neurons in the input, hidden, and output layer, respectively (Figure S9). One hidden layer is enough for handling most of the complex functions.[40] The activation function for the neurons in the hidden layer is a tangent-sigmoid function (Equation S28). The output layer of each network value represents two metrics (LCOE−LCOW, η_{PB}−PerR, and $\eta_{\text{II,system}}$−SolarPerR for each one).

The Levenberg−Marquardt backpropagation learning algorithm was used for training. This supervised learning algorithm minimizes the least square error for nonlinear functions, of each network, comparing the predicted and desired output values with high accuracy and speed.[19] Once training is complete, if the R^2 value is higher than 99%, the process continues, and a prediction function is created (three in total, one per each network). If R^2 is lower than 99%, the number of neurons in the hidden layer increases, and the training restarts. A multiobjective optimization using genetic algorithms with defined numerical boundaries optimizes each prediction function creating a Pareto front for each one. Each set of optimal parameters is tested on the thermodynamic model to ensure feasible results during validation. This process is necessary to address the possible errors in training and final prediction. If the set of optimal parameters provides unfeasible solutions, the optimization upper boundary decreases, and the multiobjective optimization restarts. After reaching feasible solutions in the final validation process, the optimization process is complete.

■ RESULTS AND DISCUSSION

The multiobjective optimization of each of the three predictive functions obtained from the neural network training represents an optimization focus for the cogeneration system (focus on optimizing economic, standalone block, or overall system performance). We divide this section into three parts to analyze each of these optimizations schemes separately. We study the variation of the optimal metrics through a Pareto front analysis (Figures 3, 5, and 7), and then, for the Pareto front, we explored the sensitivity that each system property (PR, RF, X_n, T_n) had for optimal metrics. This is accomplished through monitoring the optimal metrics and how each property varied during the optimization process (Figures 4, 6, and 8). Each one of the points in the Pareto front has an associated vector of system properties (optimal operational parameters). If the system property or metric remain fixed (small variation along the x-axis with variation in the y-axis or small variation in the y-axis with variation in the x-axis), then

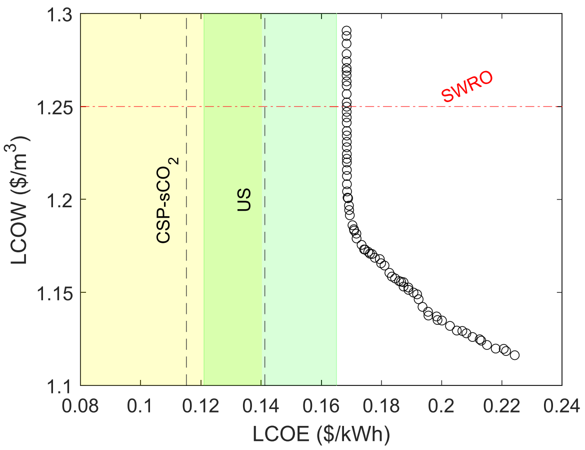

Figure 3. Pareto front for levelized costs of water and energy. The constant green area represents the range for North, South, West, and East region average energy prices in the United States, national average shown in the black dotted line. The yellow area represents the range of LCOE for other CSP sCO$_2$ found in the literature with the average shown in the black dotted line. The constant horizontal line corresponds to LCOW for the current reverse osmosis (SWRO) price in Saudi Arabia.[43]

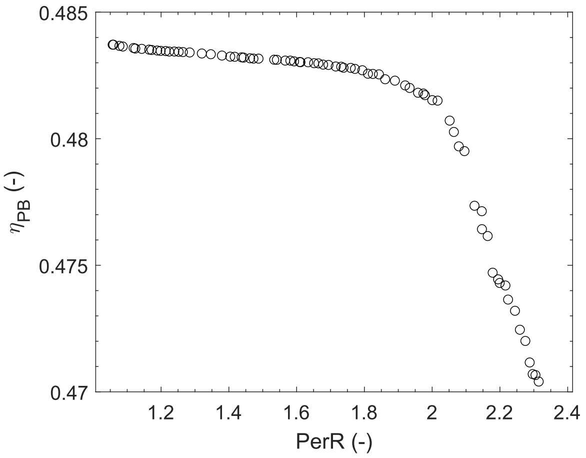

Figure 5. Pareto front for power block efficiency and desalination block performance ratio.

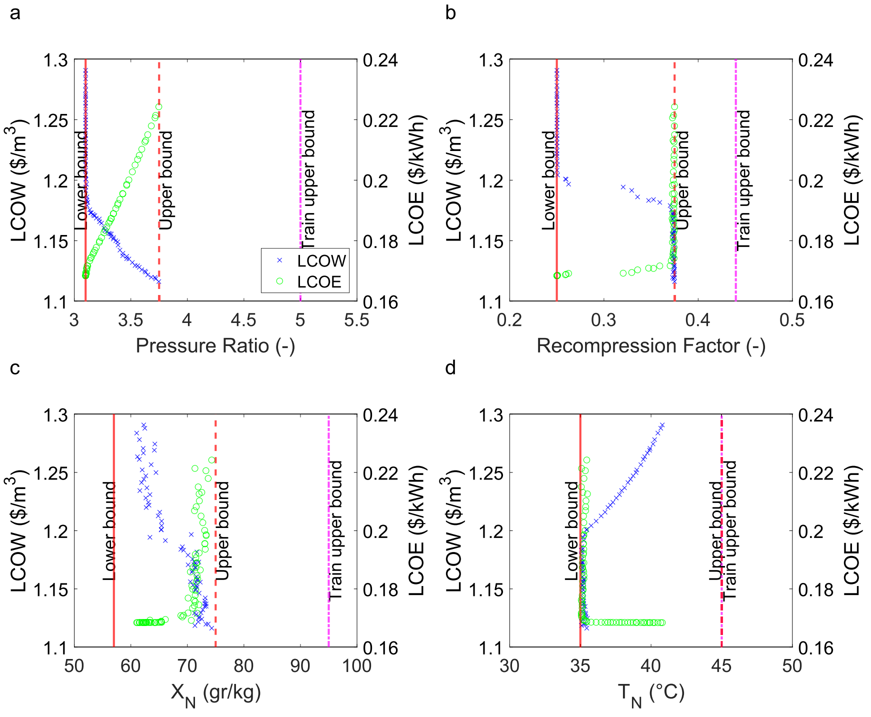

Figure 4. Optimal values of (a) pressure ratio, (b) recompression factor, (c) brine salinity, and (d) last effect temperature for the levelized cost Pareto front. The upper boundary for optimization is lower than the training upper boundary in power block parameters to achieve realistic results.

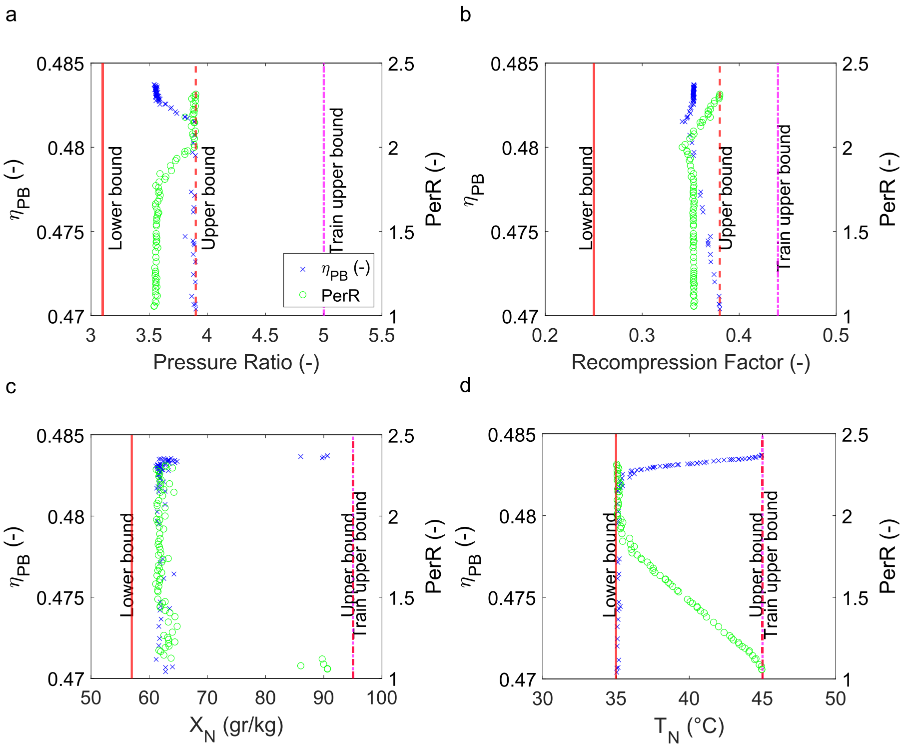

Figure 6. Optimal values of (a) pressure ratio, (b) recompression factor, (c) brine salinity, and (d) last effect temperature for the block performance Pareto front. The upper boundary for optimization is lower than the training upper boundary in power block parameters to achieve realistic results.

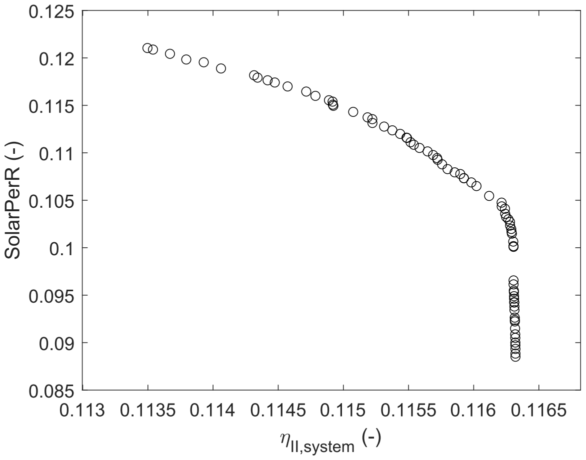

Figure 7. Pareto front for second law efficiency and solar to water performance ratio for the cogeneration system.

the optimal metric was not sensitive to that system property, but the fixed value allows for other system properties to vary altering the system metric value. On the contrary, large property changes (large variation along the *x*-axis and *y*-axis) are an indicator that the system property had a significant impact on one or both performance metrics considered. However, the four subfigures must be considered simultaneously and not as the influence of only one parameter in both optimal metrics.

Cogeneration Plant Cost Optimization. State-of-the-art CSP sCO_2 recompression Brayton cycles achieve an LCOE of 0.08−0.14 \$/(kW h) (yellow shaded region in Figure 3). The price range is largely due to variable solar collection, and different heat rejection configurations. The current price goal which would enable CSP-sCO_2 recompression Brayton cycles to become a reality (DOE Sunshot goals) is an LCOE of 0.05 \$/(kW h).[41] When the CSP power plant is combined with a thermal desalination plant, the combined system is termed a cogeneration system as power and water are produced simultaneously on-site. With the cogeneration configuration (Figure 1), the LCOE increases by almost 2× to between 0.17 and 0.22 \$/(kW h) (Figure 3). This increase in the LCOE is expected as the addition of the desalination and integration block increases the capital cost of the system and alters the power cycle heat rejection. In the conventional Brayton cycle without MED, heat rejection can occur in a single gas cooler device. Conversely, within the cogeneration system with MED, heat must be rejected to two printed-circuit heat exchangers. This difference in how heat exchange occurs specifically alters the correlations in capital expenditure estimations (Equation S23).

Despite the increase in the LCOE with the cogeneration-MED plant, the LCOW from the CSP sCO_2 recompression Brayton cycle with MED varies from 1.12 to 1.29 (\$/m^3) (Figure 3). The LCOW from the combined power and water system is lower than the specific LCOW reported from solar-driven multistage flash plants (1.81 \$/m^3) and solar-driven seawater reverse osmosis systems (SWRO) (1.25 \$/m^3).[42,43] This signifies that, in terms of solar-desalination systems, the CSP sCO_2 recompression Brayton cycle with MED can potentially exceed alternative solar-desalination technologies in terms of LCOW. It is worthwhile to note that the solar-desalination cost for the CSP-Brayton-MED system is still more expensive than fossil thermal desalination plants or fossil membrane desalination plants. For reference, utility scale fossil-driven MSF systems produce water ranging from 0.52 to

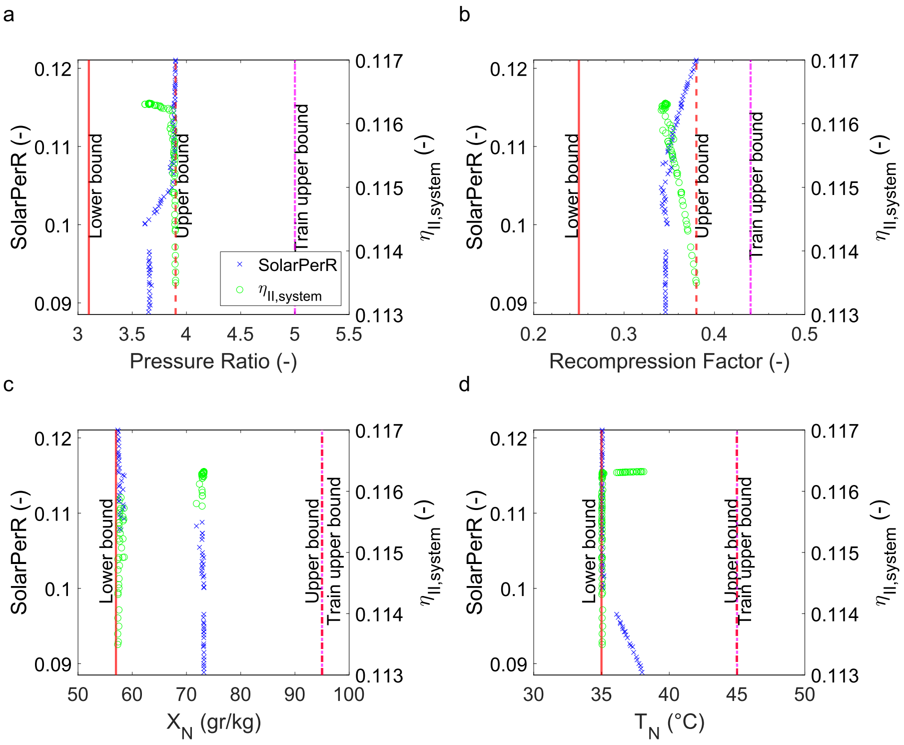

Figure 8. Optimal values of (a) pressure ratio, (b) recompression factor, (c) brine salinity, and (d) last effect temperature for system performance Pareto front analysis. The upper boundary for optimization is lower than the training upper boundary in power block parameters to achieve realistic results.

1.5 \$/m^3, and fossil powered SWRO produces water ranging from 0.45 to 1.72 \$/m^3.[3,44]

For the CSP sCO$_2$ recompression Brayton cycle with MED to attain LCOW which approaches fossil-driven desalination systems, the operational temperatures need to be altered. This can be attained through increasing the first effect temperature, or decreasing the bottom brine temperature. In addition, emphasis must be placed on economical heat exchange processes. One potential avenue which has yet to be explored in depth which could potentially achieve these design goals is the use of hybridized desalination systems which optimally operate at various temperature ranges. However, care would need to be taken to ensure that hybridization can be done without expense adding to the capital cost.

Ideally, optimizing both LCOE and LCOW is necessary for the cogeneration plant. This point is located at the corner of the Pareto curve (Figure 3). Here, the LCOE is 0.17 \$/(kW h), and the LCOW is 1.18 \$/m^3. The trade-offs in minimum LCOE and LCOW are due to the fact that the minimum LCOW coincides with the maximum water produced (50 kg/s), and the minimum LCOE corresponds with the minimum power production (106 MW) (Figure S12a,b). Both of these boundary conditions on the power and desalination system cannot be maintained at the same time. Thus, operating at the optimal cost location will require the system to operate below the optimal performance (power and water production) point. The predicted costs by the ANN compared with the thermodynamic model had a mean absolute error of 0.01% and 0.25% for the LCOE and LCOW (Figure S10a).

Variation and Influence of System Design Parameters on Optimal Cost for the Cogeneration Plant. During validation of the multiobjective optimization results obtained through EES, all training bounds were checked to ensure that the laws of thermodynamics were not violated, and if the bounds violated the first or second law, they were reduced. For this reason, the upper bound for PR decreased from 5 to 3.75, the upper bound for RF decreased from 0.44 to 0.375, and the upper bound for X_N decreased from 95 to 75 g/kg (or 95 000 to 75 000 PPM). The upper bound for T_N did not violate the laws of thermodynamics and thus coincided with the training bound (Figure 4).

PR was found to influence both economic metrics (LCOW and LCOE). A PR greater than 3 increased the optimal LCOE linearly from 0.17 to 0.224 \$/(kW h) and decreased the LCOW to 1.11 \$/m^3 (Figure 4a). Increasing RF from 0.26 to 0.36 decreased the LCOW to 1.18 \$/m^3 but had little impact on the LCOE or PR (PR = 3.1). For RF values between 0.36 and 0.375, the LCOW further decreased to 1.11 \$/m^3 while LCOE increased from 0.172 to 0.224 \$/(kW h) (Figure 4b). As PR and RF increase, it surpasses its optimum value producing the least power and increasing the amount of waste heat flowing into the desalination block.

Exit brine salinity (X_N) was found to have a higher influence in LCOW than LCOE (Figure 4c). LCOW remains less than 1.2 \$/m^3 for brine salinity ranging between 70 and 75 g/kg. Increasing the brine salinity range between 70 and 75 g/kg however resulted in the LCOE increasing from 0.17 to 0.224 \$/(kW h). For brine salinity below 70 g/kg, LCOW increased to 1.29 \$/m^3, and LCOE decreased to 0.169 \$/(kW h). Thus, a brine salinity range from 69 to 72 g/kg, and recovery ratio between 51% and 53%, should be acceptable to operate with low LCOW and LCOE (below 1.2 \$/m^3 and 0.18 \$/(kW h)). As brine salinity increases, more water is treated, and more power is consumed by the desalination block ($\dot{W}_{MED}$), which explains the increase in LCOE.

Finally, we explore the variation of T_N during the optimization process (Figure 4d). LCOW decreases from a maximum to 1.2 $/m^3 while LCOE remains constant when temperature decreases from 42 to 36 °C. From 35 to 36 °C, LCOW is 1.2 $/m^3, and LCOE decreases to 0.17 $/(kW h). Since T_N principally influences the performance of the condenser in the desalination block, it does not alter the power block costs. Therefore, decreasing the temperature of the desalination block aids in producing more affordable water. The different LCOW for lower T_N is due to the influence of the other three system properties (PR, RF, and X_N) in the optimal solution, which influence directly the amount of heat rejected in the integration block and the feedwater treated. The variation of PR and RF also explains the LCOE for different T_N.

Block Performance Metrics Optimization for the Cogeneration Plant. In addition to the cost, the individual subsystem performance is critical to enable system development. Here, the subsystems are the sCO$_2$ Brayton cycle and the MED system, and the performance values are the thermal efficiency of the power block (η_{PB}) and the performance ratio (PerR) of the MED. The η_{PB} only varied from 47% to 48.3% during the optimization process (Figure 5). This efficiency is in the range of the state-of-the-art CSP sCO$_2$ recompression Brayton cycles.[21,45] The desalination block PerR for the same parameter space ranged from 1.06 to 2.31. Thus, PerR varies by more than 2× η_{PB} while the power block remains nearly unchanged. The variation in PerR is due to the decrease in the last effect temperature, which does not affect the thermal efficiency of the power block (Figure 6d). After reaching the minimum possible temperature, PerR increases to 2.5, while the thermal efficiency drops to only 47%. This corresponds to when PR and RF reach the upper bound value (Figure 6a,b). In terms of production, η_{PB} and PerR are linearly correlated with power and water production. The maximum power production (112.6 MW) coincides with the minimum performance ratio (PerR = 1), and the maximum water production (54 kg/s) coincides with the minimum thermal efficiency indicating a direct trade-off (Figure S13).

The predicted performance by the ANN compared with the thermodynamic model alone had a mean absolute error of 0.03% and 0.25% for η_{PB} and PerR (Figure S10b). During validation of the multiobjective optimization results in EES, the upper bound decreases from 5 to 3.9 for PR and from 0.44 to 0.39 for RF due to unfeasible results.

Variation and Influence of System Design Parameters on Optimal Block Performance Metrics for the Cogeneration Plant. The small variation of η_{PB} is due to the nonparasitic integration between cogeneration system blocks, making thermal efficiency only dependent on operational parameters which influence heat rejected (Figure 6). Under the block performance optimization scheme, a minimal PR of 3.5 corresponds to the maximum η_{PB} and minimum PerR. This is due to a more efficient power block, where less heat is dissipated to the desalination block. This ultimately reduces the top brine temperature and therefore the water production. In the pressure ratio range 3.5−3.8, η_{PB} decreases linearly while PerR increases to 2. For PR above 3.8, η_{PB} drops from 48% to 47% while PerR increases from 1.96 to 2.31 (Figure 6a). Even when the η_{PB} drop is higher for PR above 3.8, the change is only 1.3% compared with the maximum achievable, while PerR doubles within the same parameter space. A strong relation exists between the optimal RF and PR under the block performance optimization scheme, from the minimal value of 0.34; as RF increases, for PR values below 3.8, PerR remains above 2 reaching the maximum value of 2.31 when RF and PR are 0.39 and 3.9. On the other hand, for RF values above 0.36, η_{PB} decreases below 48% with PR above 3.8 (Figure 6b).

Maximum η_{PB} and PerR are achieved for X_N around (meaning a recovery ratio of about 46%) making this value optimal for the cogeneration system (Figure 6c) and not a main influence in block performance. However, optimal PR and RF differ for η_{PB} and PerR. While for maximum η_{PB} PR and RF are 3.55 and 0.36, for maximum PerR theses values are 3.9 and 0.39. In consequence, under the block performance optimization scheme, the power block parameters (PR and RF) are the most influential in the cogeneration system. Decreasing T_N influences the system directly allowing the production of more water and increase of PerR; this will vary the values of PR and RF in order to consider point with maximum PerR, and as a consequence, η_{PB} decreases. However, the decrease is almost negligible for temperatures ranging from 36 to 45 °C (Figure 6d). Under this optimization scheme, a reduction of T_N is most influential in PerR, while X_N remains constant. Thus, η_{PB} is affected by PR and RF, affecting also PerR of the desalination block varying the top brine temperature and available waste heat, while T_N affects mainly PerR decreasing the bottom brine temperature.

System Performance Metrics Optimization for the Cogeneration Plant. $\eta_{II,system}$, according to eq 6, depends only on the exergy of the products from the power and desalination blocks (power production and exergy of the freshwater produced). This is due to the assumption of a fixed exergy input. Here, the total variation of the optimal $\eta_{II,system}$ is almost negligible varying from 11.3% to 11.6% (Figure 7). The nonparasitic integration scheme of the cogeneration system and the relative size of each block explain this. The power production is the most influential term, as it is 3 orders of magnitude higher than distillate exergy. During the multiobjective optimization process, power production variation is small, and maximum efficiency coincides with the maximum power production (112.4 MW) having a linear relation, while water production is 46 kg/s in this point. Water production can increase to 54 kg/s when the second law efficiency decreases to 11.32% (and power to 109 MW h) (Figure S14a).

Variation and Influence of System Design Parameters on System Performance Metrics for the Cogeneration Plant. SolarPerR is a direct function of water produced having a linear relation (eq 9) and varying from 0.088 to 0.121 when water production varies from 39 to 54 kg/s (Figure S14b). From Pareto front analysis, SolarPerR increases from 0.88 to 0.105 while $\eta_{II,system}$ remains at 11.6% and power production above 112 MW. Increasing SolarPerR to 0.121 reduces $\eta_{II,system}$ to a minimum of 11.32% and power production to 109 MW h. This little impact in the nonparasitic cogeneration system efficiency allows for the maximization of SolarPerR and freshwater production, with a negligible impact in second law efficiency.

The predicted performance by the ANN compared with the thermodynamic model in EES had a mean absolute error of 0.01% and 0.015% $\eta_{II,system}$ and SolarPerR (Figure S10c). During validation of the multiobjective optimization results in EES, the upper bound decreases from 5 to 3.9 for PR and from 0.44 to 0.38 for RF due to unfeasible results. For this Pareto front (Figure 7), we also explore the variation of each system property (PR, RF, X_N, T_N) during the optimization process to identify their influence in the cogeneration system (Figure 8). Altering PR from 3.6 to 3.8 has an almost negligible impact on $\eta_{II,system}$ while in this range SolarPerR varies from 0.088 to 0.105. When PR increases from 3.8 to 3.9, SolarPerR increases to 0.121 while $\eta_{II,system}$ decreased to 11.35% (Figure 8a). When RF increases from 0.35 to 0.38, $\eta_{II,system}$ decreases linearly, while SolarPerR increases linearly. This trade-off is due the direct relation between RF and power and water production. A higher value increases the heat rejected by the power block allowing the production of more freshwater in the desalination block. As RF increases, η_{PB} of the power block decreases with power production and, in consequence, second law efficiency (Figure 8b).

X_N achieves two possible values 58 and 73 g/kg showing an inverse relation between $\eta_{II,system}$ and SolarPerR (Figure 8c). For X_N = 73 g/kg, $\eta_{II,system}$ reaches the maximum value (11.6%); this is due to the fact that when X_N is higher, the cogeneration system produces more power and less freshwater. Keeping X_N below 60 g/kg increases SolarPerR to the maximum value (0.12). By consequence, the cogeneration system produces more water when the recovery ratio of the plant is about 40%. T_N variation is similar to the block Pareto front analysis. Decreasing T_N from 38 to 36 °C did not influence $\eta_{II,system}$ (11.6%). However, SolarPerR increases from 0.09 to close to 0.1 (Figure 8d). A lower value for T_N maximizes water production and SolarPerR, due to increases in the operational temperature range of the MED system. Exploration of system properties during cogeneration system performance optimization allows one to conclude that a design focused on maximizing water production in the system proposed, i.e., operating at higher PR and RF and lower X_N and T_N, will have almost negligible impact on $\eta_{II,system}$ when compared with a configuration focused on maximizing power production.

CONCLUSIONS

A thermodynamic and economic analysis aided by the artificial neural network (ANN) was performed to evaluate a cogeneration CSP sCO_2 Brayton cycle with MED plant. Optimal system performance and cost were determined, and three trade-offs were examined (LCOE−LCOW, η_{PB}−PerR, and $\eta_{II,system}$−SolarPerR). For all simulations, ANN predictions had a maximum mean absolute error of 0.25% when compared with the thermodynamic model simulated with traditional thermodynamic solvers (EES). The use of the ANN for optimization aided in addressing computational resource consumption challenges due to the complexity of the complete system thermodynamic model. From a solar−thermal desalination perspective, there are significant opportunities for achieving high power and water production from CSP-sCO_2 Brayton MED cogeneration plants. Furthermore, the LCOW may be able to approach 1.25 \$/m^3 indicating that the cost of competitive water and power may be able to begin to compete with fossil-based alternatives.

ASSOCIATED CONTENT

Supporting Information

The Supporting Information is available free of charge at https://pubs.acs.org/doi/10.1021/acsestengg.0c00132.

Energy balance equations and cost correlations per device along with additional supportive results, like validation and error estimation (PDF)

AUTHOR INFORMATION

Corresponding Author

Marta C. Hatzell − *George W. Woodruff School of Mechanical Engineering, Georgia Institute of Technology, Atlanta, Georgia 30332-0405, United States;* orcid.org/0000-0002-5144-4969; Phone: +1 (404) 385 4503; Email: marta.hatzell@me.gatech.edu

Authors

Rodrigo A. Caceres Gonzalez − *George W. Woodruff School of Mechanical Engineering, Georgia Institute of Technology, Atlanta, Georgia 30332-0405, United States;* orcid.org/0000-0003-3682-6130

Yanjie Zheng − *Department of Mechanical Engineering, Vanderbilt University, Nashville, Tennessee 37235-1826, United States*

Kelsey B. Hatzell − *Department of Mechanical Engineering, Interdisciplinary Material Science Program, and Chemical and Biomolecular Engineering, Vanderbilt University, Nashville, Tennessee 37235-1826, United States;* orcid.org/0000-0002-5222-7288

Complete contact information is available at: https://pubs.acs.org/10.1021/acsestengg.0c00132

Notes

The authors declare no competing financial interest.

ACKNOWLEDGMENTS

The authors gratefully acknowledge the funding support of CONICYT PFCHA/DOCTORADO BECAS CHILE/2018-72190312. This material is based upon work supported by the National Science Foundation under Grant 1821843 and 1821573.

REFERENCES

(1) Luo, T.; Young, R.; Reig, P. *Aqueduct projected water stress rankings*; Technical note for World Resources Institute: Washington, DC, 2015. http://www.wri.org/publication/aqueduct-projected-water-stress-country-rankings.

(2) Ullah, I.; Rasul, M. Recent Developments in Solar Thermal Desalination Technologies: A Review. *Energies* **2019**, *12*, 119.

(3) Rao, P.; Aghajanzadeh, A.; Sheaffer, P.; Morrow, W. R.; Brueske, S.; Dollinger, C.; Price, K.; Sarker, P.; Ward, N.; Cresko, J. *Volume 1: survey of available information in support of the energy-water bandwidth study of desalination systems*; Lawrence Berkeley National Laboratory, 2016. https://escholarship.org/uc/item/4sw805r2.

(4) Al-Karaghouli, A.; Kazmerski, L. L. Energy consumption and water production cost of conventional and renewable-energy-powered desalination processes. *Renewable Sustainable Energy Rev.* **2013**, *24*, 343−356.

(5) Virgili, F.; Pankratz, T.; Gasson, J. *IDA Desalination Yearbook 2015-2016*; Media Analytics Limited, 2016.

(6) Shahzad, M. W.; Burhan, M.; Ang, L.; Ng, K. C. Energy-water-environment nexus underpinning future desalination sustainability. *Desalination* **2017**, *413*, 52−64.

(7) Elsayed, M. L.; Mesalhy, O.; Mohammed, R. H.; Chow, L. C. Exergy and thermo-economic analysis for MED-TVC desalination systems. *Desalination* **2018**, *447*, 29−42.

(8) Wellmann, J.; Meyer-Kahlen, B.; Morosuk, T. Exergoeconomic evaluation of a CSP plant in combination with a desalination unit. *Renewable Energy* **2018**, *128*, 586−602.

(9) Qiblawey, H. M.; Banat, F. Solar thermal desalination technologies. *Desalination* **2008**, *220*, 633−644.

(10) Ahmed, F. E.; Hashaikeh, R.; Hilal, N. Solar powered desalination – Technology, energy and future outlook. *Desalination* **2019**, *453*, 54−76.

(11) Shahzad, M. W.; Burhan, M.; Ng, K. C. A standard primary energy approach for comparing desalination processes. *npj Clean Water* **2019**, *2*, 1−7.

(12) Gunawan, A.; Simmons, R. A.; Haynes, M. W.; Moreno, D.; Menon, A. K.; Hatzell, M. C.; Yee, S. K. Techno-Economics of Cogeneration Approaches for Combined Power and Desalination From Concentrated Solar Power. *J. Sol. Energy Eng.* **2019**, *141*, 021004.

(13) Kouta, A.; Al-Sulaiman, F. A.; Atif, M. Energy analysis of a solar driven cogeneration system using supercritical CO2 power cycle and MEE-TVC desalination system. *Energy* **2017**, *119*, 996−1009.

(14) Linares, J. I.; Montes, M. J.; Cantizano, A.; Sánchez, C. A novel supercritical CO2 recompression Brayton power cycle for power tower concentrating solar plants. *Appl. Energy* **2020**, *263*, 114644.

(15) Turchi, C. S.; Ma, Z.; Neises, T. W.; Wagner, M. J. Thermodynamic study of advanced supercritical carbon dioxide power cycles for concentrating solar power systems. *J. Sol. Energy Eng.* **2013**, *135*, 1−7.

(16) Dostal, V.; Hejzlar, P.; Driscoll, M. J. The supercritical carbon dioxide power cycle: comparison to other advanced power cycles. *Nucl. Technol.* **2006**, *154*, 283−301.

(17) Sharan, P.; Neises, T.; Turchi, C. Thermal desalination via supercritical CO 2 Brayton cycle: Optimal system design and techno-economic analysis without reduction in cycle efficiency. *Appl. Therm. Eng.* **2019**, *152*, 499−514.

(18) Sharan, P.; Neises, T.; Turchi, C. Optimal feed flow sequence for multi-effect distillation system integrated with supercritical carbon dioxide Brayton cycle for seawater desalination. *J. Cleaner Prod.* **2018**, *196*, 889−901.

(19) Goyal, A.; Garimella, S. Computing thermodynamic properties of ammonia−water mixtures using artificial neural networks. *Int. J. Refrig.* **2019**, *100*, 315−325.

(20) Arat, H.; Arslan, O. Optimization of district heating system aided by geothermal heat pump: A novel multistage with multilevel ANN modelling. *Appl. Therm. Eng.* **2017**, *111*, 608−623.

(21) Sharan, P.; Neises, T.; McTigue, J. D.; Turchi, C. Cogeneration using multi-effect distillation and a solar-powered supercritical carbon dioxide Brayton cycle. *Desalination* **2019**, *459*, 20−33.

(22) Blair, N.; Diorio, N.; Freeman, J.; Gilman, P.; Janzou, S.; Neises, T. W.; Wagner, M. J. *System Advisor Model (SAM) General Description (Version 2017.9.5)*; NREL/TP-6A20-70414; National Renewable Energy Laboratory: Golden, CO, 2018. https://www.nrel.gov/docs/fy18osti/70414.pdf (accessed 12-05-2019).

(23) Klein, S. A. *Engineering equation solver (EES), Academic Commercial, V10, 644, Madison, USA, F-chart software*, 2018. http://www.fchart.com/ees.

(24) Sharqawy, M. H.; Lienhard V, J. H.; Zubair, S. M. Thermophysical properties of seawater: A review of existing correlations and data. *Desalin. Water Treat.* **2010**, *16*, 354−380.

(25) Nayar, K. G.; Sharqawy, M. H.; Banchik, L. D.; Lienhard, J. H. Thermophysical properties of seawater: A review and new correlations that include pressure dependence. *Desalination* **2016**, *390*, 1−24.

(26) Schroder, A. U. *A study of power cycles using supercritical carbon dioxide as the working fluid*. Ph.D. thesis, University of Cincinnati, 2016.

(27) Palenzuela, P.; Hassan, A. S.; Zaragoza, G.; Alarcón-padilla, D.-c. Steady state model for multi-effect distillation case study : Plataforma Solar de Almería MED pilot plant. *Desalination* **2014**, 337, 31−42.

(28) Alharbi, S.; Elsayed, M.; Chow, L. Thermo-Economic Analysis of an Integrated Supercritical CO2 Brayton Cycle and Multiple Effect Desalination Systems. *ASME 2018 International Mechanical Engineering Congress and Exposition* **2018**, *6B*, 1−10.

(29) Elsayed, M. L.; Mesalhy, O.; Mohammed, R. H.; Chow, L. C. Transient and thermo-economic analysis of MED-MVC desalination system. *Energy* **2019**, *167*, 283−296.

(30) Elsayed, M. L.; Mesalhy, O.; Mohammed, R. H.; Chow, L. C. Transient performance of MED processes with different feed configurations. *Desalination* **2018**, *438*, 37−53.

(31) Christ, A.; Regenauer-Lieb, K.; Chua, H. T. Thermodynamic optimisation of multi effect distillation driven by sensible heat sources. *Desalination* **2014**, *336*, 160−167.

(32) Datsgerdi, H. R.; Chua, H. T. Thermo-economic analysis of low-grade heat driven multi-effect distillation based desalination processes. *Desalination* **2018**, *448*, 36−48.

(33) Christ, A.; Regenauer-Lieb, K.; Chua, H. T. Boosted Multi-Effect Distillation for sensible low-grade heat sources: A comparison with feed pre-heating Multi-Effect Distillation. *Desalination* **2015**, *366*, 32−46.

(34) Petela, R. Exergy of Heat Radiation. *J. Heat Transfer* **1964**, *86*, 187−192.

(35) Alharbi, S.; Elsayed, M. L.; Chow, L. C. Exergoeconomic analysis and optimization of an integrated system of supercritical CO2 Brayton cycle and multi-effect desalination. *Energy* **2020**, *197*, 117225.

(36) Sarmiento, C.; Cardemil, J. M.; Díaz, A. J.; Barraza, R. Parametrized analysis of a carbon dioxide transcritical Rankine cycle driven by solar energy. *Appl. Therm. Eng.* **2018**, *140*, 580−592.

(37) Keshtkar, M. M.; Khani, A. G. Exergoeconomic analysis and optimization of a hybrid system based on multi-objective generation system in Iran: a case study. *Renewable Energy Focus* **2018**, *27*, 1−13.

(38) Zare, V.; Mahmoudi, S. M. S.; Yari, M.; Amidpour, M. Thermoeconomic analysis and optimization of an ammonia−water power/cooling cogeneration cycle. *Energy* **2012**, *47*, 271−283.

(39) Jamali, A.; Ahmadi, P.; Mohd Jaafar, M. N. Optimization of a novel carbon dioxide cogeneration system using artificial neural network and multi-objective genetic algorithm. *Appl. Therm. Eng.* **2014**, *64*, 293−306.

(40) Lv, C.; Xing, Y.; Zhang, J.; Na, X.; Li, Y.; Liu, T.; Cao, D.; Wang, F.-Y. Levenberg−Marquardt Backpropagation Training of Multilayer Neural Networks for State Estimation of a Safety-Critical Cyber-Physical System. *IEEE Transactions on Industrial Informatics* **2018**, *14*, 3436−3446.

(41) Murphy, C.; Sun, Y.; Cole, W. J.; Maclaurin, G. J.; Mehos, M. S.; Turchi, C. S. *The Potential Role of Concentrating Solar Power within the Context of DOE's 2030 Solar Cost Targets*; NREL/TP-6A20-71912; National Renewable Energy Laboratory, 2019.

(42) Pugsley, A.; Zacharopoulos, A.; Mondol, J. D.; Smyth, M. Global applicability of solar desalination. *Renewable Energy* **2016**, *88*, 200−219.

(43) Caldera, U.; Breyer, C. Learning curve for seawater reverse osmosis desalination plants: capital cost trend of the past, present, and future. *Water Resour. Res.* **2017**, *53*, 10523−10538.

(44) Rabiee, H.; Khalilpour, K. R.; Betts, J. M.; Tapper, N. *Polygeneration with Polystorage: For Chemical and Energy Hubs*; Elsevier Inc., 2018; pp 409−458.

(45) Nguyen, T. D. C.; Choe, J.; Ebiwonjumi, B.; Lemaire, M.; Lee, D. Core design of long-cycle small modular lead-cooled fast reactor. *Int. J. Energy Res.* **2019**, *43*, 254−273.